Journal of The Electrochemical Society, 2020 **167** 044519
1945-7111/2020/167(4)/044519/9/$40.00 © 2020 The Electrochemical Society ("ECS"). Published on behalf of ECS by IOP Publishing Limited

Elucidating the Role of Ionomer in the Performance of Platinum Group Metal-free Catalyst Layer via in situ Electrochemical Diagnostics

Guanxiong Wang,[=,*] Luigi Osmieri,[=,*] Andrew G. Star,[*] Jason Pfeilsticker, and K. C. Neyerlin[*,z]

National Renewable Energy Laboratory, Golden, Colorado 80401, United States of America

The ionomer content in platinum group metal (PGM)-free polymer electrolyte fuel cell (PEFC) cathode catalyst layer (CCL) plays an important role in the electrode gas transport properties, proton conductivity, and hence, membrane electrode assembly (MEA) performance. In this work, the ionomer content in the CCL is varied, influencing electrode microstructure by altering porosity, tortuosity, as well as ionomer distribution and coverage of the catalyst particles. A novel technique consisting of a H_2 pump, combined with a Pt black sensor layer, is used to measure the bulk mass transport resistance of a series of PGM-free CCL prepared with different ionomer contents. The values for bulk electrode mass transport resistance are contrasted with electrode proton transport resistance in the cathode catalyst layer, establishing a clearly defined trade-off between two key performance limiting phenomena and identifying a need for novel PGM-free electrode fabrication strategies.
 [DOI: 10.1149/1945-7111/ab7aa1]

Manuscript submitted December 29, 2019; revised manuscript received February 18, 2020. Published March 9, 2020. *This was paper 234 presented at the Atlanta, Georgia, Meeting of the Society, October 13–17, 2019.*

Supplementary material for this article is available online

Polymer electrolyte fuel cells (PEFCs) are electrochemical devices that directly convert the chemical energy of H_2 into electrical energy with high efficiency (theoretical thermodynamic efficiency as high as 83%),[1] and without polluting emissions. PEFCs are particularly interesting for automotive applications because they operate close to ambient conditions, enabling fast start-up and shut-down.[2]

In state-of-the-art PEFCs, Pt is used to catalyze both anodic hydrogen oxidation reaction (HOR) and cathodic oxygen reduction reaction (ORR).[3] Unfortunately, Pt is a costly and rare noble metal, and according to a recent breakdown study form the U.S. Department of Energy (DOE), it represents the major part of the total cost of a PEFC stack for automotive applications.[4] In recent years, several models of fuel cell vehicles (FCVs) have been commercialized by some of the main manufacturers like Daimler, Honda, Hyundai, and Toyota.[5] While presently the number of vehicles powered by PEFC systems is lower than traditional internal combustion engine-powered ones, the fleet of FCVs is expected to grow considerably in the near future due to the exponentially increasing deployment of renewable energy[6] and increased vehicle emission regulations.[7] In this scenario, Pt cost represents the main hindrance for the large-scale commercialization of FCVs.[8] Due to the slower ORR kinetics compared to HOR, most of the Pt in a PEFC is located at the cathode,[3,9] resulting in major research efforts focused on the development of innovative platinum group metal (PGM)-free catalysts with improved activity.[10] The most promising class of PGM-free catalysts are carbonaceous materials doped with nitrogen and one (or more) active 3d-period transition metals (e.g. Fe, Co, Mn).[11,12] The synthesis process for their obtainment can vary, but it always includes at least one high temperature pyrolysis, usually between 800 °C and 1100 °C.[13,14]

The literature about PGM-free catalysts synthesis, characterization, and beginning of life activity measured in rotating disk electrode (RDE) and membrane electrode assembly (MEA) is abundant.[13–15] In contrast, literature relating electrode design and resulting PGM-free electrode transport properties is less frequent.[16–18]

While variables such as catalyst loading and ionomer content certainly play an important role,[19–22] the impact of other processing variables, such as catalyst deposition method (e.g. spray coating, blade coating, hand painting, roll-to-roll coating),[23,24] ionomer spatial gradients (in-layer and through-layer),[25] ink concentration,[23,26] ink composition,[27,28] ink evaporation rate,[26] is less clear.

Consequently, the observed performance differences for PGM-free PEFCs is not only ascribed to the intrinsic activity of a catalyst, but also to active-site accessibility, aggregate level diffusion, bulk electrode mass transport properties, and proton resistance in the catalyst layer.[29,30] These properties are related to the ionomer distribution in the catalytic layer, which may vary considerably as a function of the MEA fabrication method, and the aforementioned process variables.[31] The effects of mass transport and ionic resistance in the catalyst layer are much more impactful for PGM-free vs platinum based (Pt/C) electrodes, due to the higher loadings, and nearly 10× thicker electrodes, necessary to obtain acceptable power densities.[32,33] Thus, it is easy to understand the importance of the electrode layer design to ensure a good PGM-free based electrode performance.

Catalyst porosity, agglomerate size, and ionomer distribution in relation to the catalyst particles dictate the gas transport resistance within the electrode.[34] Electrode layer mass transport resistance can be separated into pressure dependent resistances, due to molecular diffusion, and pressure independent resistances, resulting from Knudsen diffusion in small pores and a solid-state diffusion process through ionomer films, which is pressure independent.[35] For thick PGM-free it is more critical to isolate the contributions of transport resistance at the aggregate/agglomerate level (i.e. up to the active site) from resistances through the electrode bulk, enabling informed directions for future research. While the use of HOR or ORR limiting current techniques applied at different pressures have proven useful to quantify the pressure dependent and independent components of the mass transport resistance of the catalyst layer,[35–37] in their current forms they require complex models to separate out bulk electrode and aggregate level transport resistance. Abundant literature exists about mass transport resistance calculations in PEFC Pt/C cathode catalyst layers,[38–41] looking at different aspects such as bulk diffusion resistance, and local resistances at Pt-ionomer interface. For low loading Pt/C catalysts systems, it has been pointed out that the local O_2 transport resistance at the Pt-ionomer interface is the limiting factor for performance at high

[=]These authors contributed equally to this work.
[*]Electrochemical Society Member.
[z]E-mail: kenneth.neyerlin@nrel.gov

current densities.[19] For PGM-free catalysts, this issue is less likely to be a limiting factor for two main reasons. First, the PGM-free CCLs are usually 10 times thicker than their Pt/C counterparts.[32] Second, the ORR activity of these materials is lower, and the active sites are more homogeneously distributed on the whole catalyst surface (atomically dispersed Fe-N_x sites vs Pt metal nanoparticles). This makes the bulk molecular diffusion through macro-mesopores, and the Knudsen diffusion through micropore to be proportionally more impactful than the local diffusion through the ionomer/catalyst interface for PGM-free catalysts. For this reason, the mass transport resistance measurement based on H_2 limiting current is an interesting and useful approach to be investigated.

Furthermore, although in situ electrochemical diagnostics techniques like cyclic voltammetry (CV) and electrochemical impedance spectroscopy (EIS) can be correlated, respectively, to the interaction between catalyst and ionomer,[42,43] and the proton resistance in the catalyst layer,[44,45] they are best utilized as complementary techniques to fully describe electrode level interactions.

Successful PGM-free PEFC development must include device-level studies and microstructure optimization, especially for minimizing the concentration overpotential in the thick PGM-free catalyst layers (CL). In this work, we utilize our recently published hydrogen limiting current measurement approach to determine in situ the mass transport resistance in the cathode catalyst layer (CCL),[46] to investigate the influence of ionomer content on the performance of MEAs fabricated using a commercially available PGM-free Fe-N-C catalyst. The MEAs are examined as a function of relative humidity (RH) to establish the influence of proton resistance and bulk electrode gas mass transport resistance in the CCL on the MEA performance, helping to elucidate fundamental electrode level properties and guide ongoing research and development in both catalyst synthesis and MEA fabrication.

Experimental

Materials.—All MEAs were fabricated using membrane Nafion® 211 (DuPont). A desired amount of Nafion® ionomer (DE2020, Ion Power Inc.) was used in the electrode. 47.2 wt% Pt on high surface carbon catalyst (Pt/HSC, TEC10E50E, TKK) is used as a reference electrode and anode material in the H_2 pump experiments and MEA tests. Platinum black (TEC90300, TKK) was used to fabricate the Pt sensor layer. The PGM-free catalyst used in this work was a commercial Fe–N–C material with 10 nm average pore size (PMF-011904, Pajarito Powder, LLC). Toray 060 carbon paper with 5% wet-proofing was used as diffusion media for mass transport resistance measurements, and SGL 29BC carbon paper was used for fuel cell performance tests. Virgin skived PTFE gaskets (Enflo) was used to seal the active area. Ultrapure Millipore 18 MΩ deionized water and ultra-high purity gases (General Air, Commerce City, Colorado, USA) were used for all experiments.

MEA fabrication.—PGM-free cathode catalyst inks were made by mixing n-propanol and deionized water (at a volume ratio of 2:1) having a catalyst concentration of ca. 8 mg ml^{-1}. A desired amount of ionomer was then added to obtain 15, 30, 35, 40 and 45 wt% ionomer content in the dry electrode. The resulting ink was sonicated for 60 min in an ice bath.

The anode inks consisted of a mixture of deionized water and n-propanol (at a volume ratio of ~4:3) having a catalyst (47 wt% Pt/HSC-TKK) concentration of ca. 2 mg ml^{-1}, and an ionomer to carbon ratio of 0.9. The anode ink was horn-sonicated for 20 s in an ice bath to break up the secondary particles, and then sonicated in an ice bath for 20 min.

As previously published,[46] Pt black (PtB) layers were made from inks containing deionized water and n-propanol (at a volume ratio of 4:3) having a catalyst concentration of ca. 2 mg ml^{-1}. The PtB inks did not included ionomer. The ink was horn sonicated for 2 min in an ice bath to break up the secondary particles, followed by sonication in an ice bath for 60 min.

All inks were subsequently coated on Nafion® 211 membranes heated to 80 °C on a porous hot plate with vacuum applied. All catalyst coated membranes (CCMs) were fabricated in-house using a Sono-Tek ultrasonic spray coating system equipped with either a 25 kHz (for Pt/C catalyst inks) or 48 kHz (for Fe-N-C catalyst inks) "accumist" type nozzle. Two different nozzles were used for PGM-free and Pt/C catalysts spraying to avoid any Pt contamination on PGM-free catalyst layers. A Pt loading of 0.2 mg_{Pt} cm^{-2} was used for the anode for all MEAs. For HOR limiting current measurements, the PtB loading on the electrode was 0.8 mg_{Pt} cm^{-2}. This electrode was used as working sensor layer. For the MEAs used for the HOR limiting current measurements, after spraying the PtB layer on the cathode side, the PGM-free CL was sprayed onto the PtB layer.

The PGM-free catalyst loading was measured calculating the difference between the weight of the CCM before and after the spray process. A thickness measurement of the PGM-free catalyst was also done using a micrometer, as an indirect method to estimate the catalyst loading (assuming a carbon density of ca. 0.4 g cm^{-3} in the final electrode).[32] These two methods resulted in PGM-free electrocatalyst loadings of 2 mg cm^{-2} ± 5% for all electrodes tested here.

The Pt loading for all Pt-containing catalyst layers was verified by X-ray fluorescence spectroscopy (XRF) using a Fischer FISCHERSCOPE® X-ray XDV®-SDD instrument.

Once fabricated, the CCMs with PtB sensor layer, to be used for HOR limiting current experiments, were sandwiched between two T060 gas diffusion layers (GDLs) and positioned into a 5 cm^2 differential cell hardware for H_2 oxidation limiting current density measurements. PTFE gaskets were selected with a thickness such that the final compression of the GDL was 20%, and the fuel cell hardware was tightened to 4.50 Nm torque.

The CCMs without PtB sensor layer, to be used for polarization curves performance tests, were sandwiched between two SGL 29BC GDLs and assembled into a 5 cm^2 differential cell hardware selecting PTFE gaskets to achieve 25% compression of the GDL, and the fuel cell hardware was tightened to 4.50 Nm torque.

Fuel cell testing.—All MEA tests were carried out using a 14-channel straight parallel flow field,[35] using high stoichiometry to be under differential cell conditions. HOR limiting currents were measured by CV, flowing a gas mixture of 5% H_2 in N_2 on both anode and cathode with a flow rate of 2 and 5 l min^{-1}, respectively. Before measuring the HOR limiting current, the cell was conditioned using a customized Hydrogenics fuel cell test station to fully activate the PtB layer.[47] The HOR limiting current measurements were done at 80 °C, and at different RH and pressure values. The RH used were 50, 75, 90, and 100%. At each RH, different total cell pressures of 150, 200, 250, and 300 kPa were applied. The variations in H_2 gas concentration with varying RH due to the higher water vapor fraction were considered in the calculation of the mass transport resistance. Background CVs for capacitive current contribution subtraction, were also measured at the same operating conditions, flowing N_2 in the working electrode. A Teledyne Medusa fuel cell test station was used to control temperature, pressure, gas flows, and RH. A Metrohm Autolab potentiostat (Model PGSTAT302N) was used for the CV measurements. CVs were measured at 40 mV s^{-1} scan rate between 0.05 and 0.80 V, using a Metrohm Autolab potentiostat (Model PGSTAT302N). When voltage increased, the current density reached a plateau value at high voltages, and after the capacitive background correction, the plateau value was taken as limiting current.

Fuel cell polarization curve tests were done on a customized Hydrogenics fuel cell test station. A set of polarization curves, using O_2 (99.99% pure) and air on the cathode, were measured at 80 °C, at two different RH values of 75 and 100%. The total gas pressure was 150 kPa on both anode and cathode. All the polarization curves were recorded in voltage-control mode in the anodic scan direction, from 0.30 V to the open-circuit voltage (OCV), with a 50 mV potential step from 0.3 to 0.5 V, and with 25 mV potential step from 0.5 V to OCV, holding each potential for 75 s. The reported current density values are the average of the last 60 s of each potential hold.

CVs were measured at 80 °C at different RH values of 60, 75, 90, and 100%, under H_2/N_2 (anode/cathode flows, 100 cm^3 min^{-1}) at 100 kPa gas partial pressure between 0.0 and 1.0 V vs SHE with a scan rate of 20 mV s^{-1} using an Autolab potentiostat (Model PGSTAT302N), to determine the capacitance changes of the PGM-free electrodes in function of RH.

EISs were also measured in the same conditions at a cell potential of 0.2 V vs SHE (3 mV signal amplitude), between 10,000 and 0.1 Hz to determine the variations of the proton resistance in the CCL in function of RH. The intercept of the EIS Nyquist plot with the real axis, where the phase angle is zero, represents the sum of membrane protonic and cell electronic bulk and contact resistances, and is indicated as the high-frequency resistance (HFR or R_Ω^{HFR}). This value was used to correct the polarization curves from the contribution of the HFR.

The EIS obtained Nyquist plots were fitted to a previously developed transmission line model[30] (see the equivalent circuit of the model shown in Fig. S1 in the Supplementary Material available online at stacks.iop.org/JES/167/044519/mmedia), to calculate the proton resistance in the CCL.

Results and Discussion

Fuel cell performance test.—Having a sufficiently high ionomer loading is important to lower the proton resistance of the CCL, which is necessary to achieve good fuel cell performance, though the optimum ionomer content may depend on the specific fabrication method (ink formulation and deposition method).[24,31,48]

Due to the considerable thickness of PGM-free electrodes (ca. 100 μm, about 10 times more than a Pt/C based electrode), increased ionomer content often results in increasing mass transport resistances through the electrode itself, limiting performance at high current density.[16–18] This is an additional resistance beyond what is typically seen for thinner Pt based electrodes where the focus is on aggregate level and local transport losses near the Pt surface.

For this study, MEAs were fabricated using the same PGM-free catalyst in the cathode electrode, but with ionomer contents of 30, 35, 40 and 45 wt%, respectively. All cathode electrodes had the same catalyst loading of 2 mg cm^{-2} ± 5%.

Figures 1a–1b shows the H_2/O_2 polarization curves corrected for the HFR ohmic contribution at 100% and 75% RH, respectively. At 100% RH, the MEA with 35 wt% ionomer performs better, while the other MEAs show a lower performance, very similar to each other. Only the MEA with 30 wt% ionomer slightly outperforms the other two at high current density (see Fig. 1a). However, at 75% RH the MEA with 45 wt% ionomer performs the best. While there is clearly an "optimum" ionomer content for this particular fabrication method and electrocatalyst, it's difficult to isolate the relative voltage loss contributions stemming from proton and gas transport from a polarization curve alone. Furthermore, the "optimum" ionomer contents will shift depending on whether the cell is operated in O_2 or air.

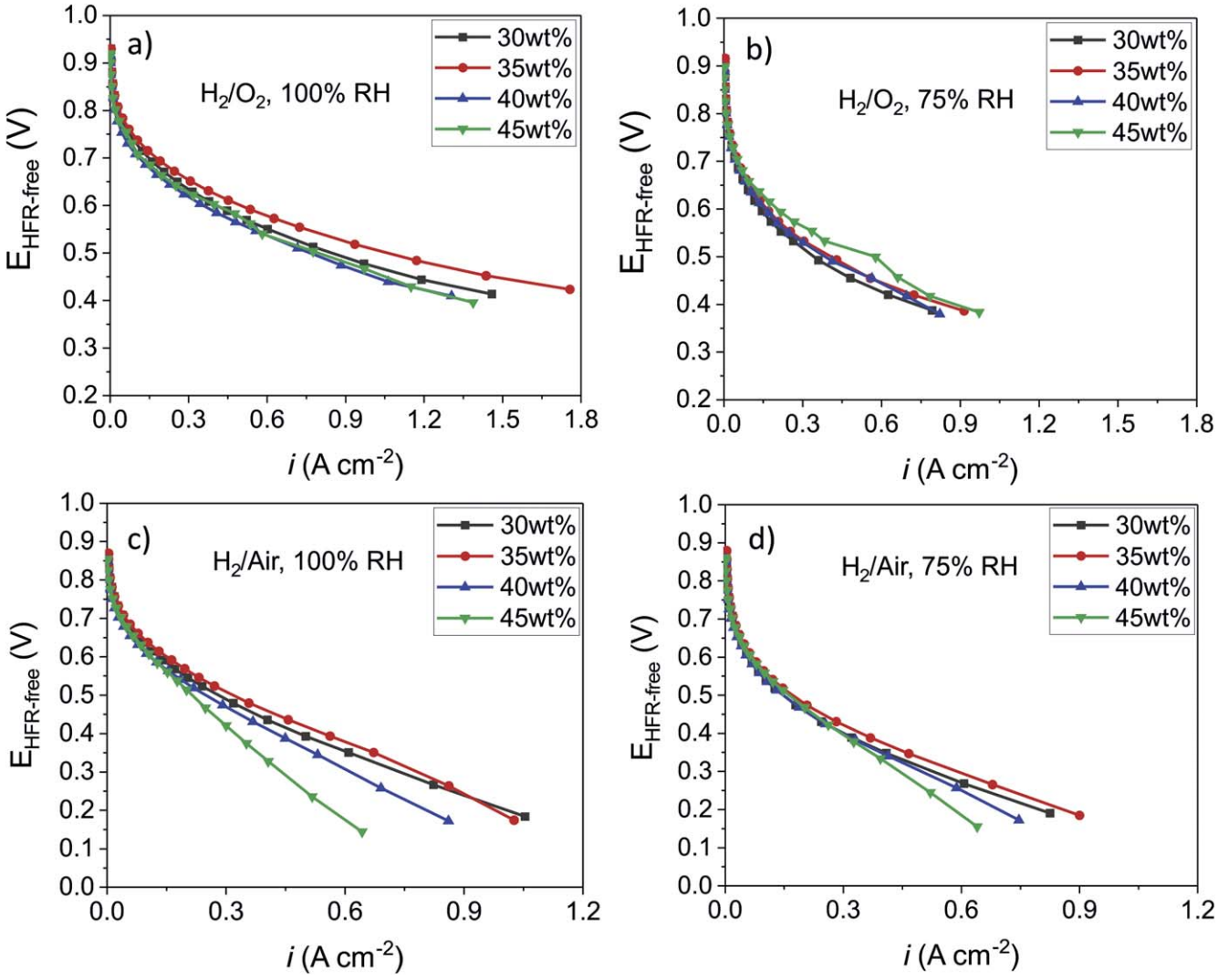

Figure 1. Polarization curves corrected for the HFR contribution, measured at 80 °C and 150 kPa for electrodes with different ionomer loadings: (a) H_2/O_2, 100%RH; (b) H_2/O_2, 75%RH; (c) H_2/Air, 100%RH; and (d) H_2/Air, 75%RH.

The HFR-corrected H_2/air polarization curves at 100% and 75% RH are depicted in Figs. 1c–1d. Operating under H_2/air, the MEA with 35 wt% ionomer gives the best performance, and 45 wt% the worst. In contrast to H_2/O_2 operation, beyond ca. 0.3 A cm^{-2} there is clear divergence in performance at both 100% and 75% RH, with the 45 wt% MEA being by far the lowest performing.

While intuitively these results could be explained by a combination of proton conduction and gas mass transport in the electrode, further investigation using in situ electrochemical diagnostics are necessary to elucidate the electrode level interactions and phenomena responsible for range of observed performances.

Cyclic voltammetry.—CVs for electrodes fabricated with 30 and 45 wt% ionomer are shown in Figs. 2a–2b (see Figs. S2a–S2b in the SI for 35 and 40 wt%). From the capacitive responses of the CV, information regarding catalyst surface chemistry as well as the electrode level interactions, specifically those between ionomer/electrocatalyst or water/electrocatalyst, can be obtained. The shape of the CVs in Figs. 2a–2b and S2a–S2b is quasi-rectangular, denoting that the main contribution to the capacitive current comes from the electrostatic charge and discharge of the double layer.[42,43,49] However, the pseudo-capacitance contribution must also be considered. The pseudo-capacitance is due to the presence of N- and O-containing functional groups on the surface of the catalyst, which can undergo to chemisorption phenomena with partial charge transfer, and to redox processes (as the quinone–hydroquinone).[42,43,50,51] In the potential region between 0.70 and 0.85 V, a small reversible peak is observed. This peak is attributable to the redox behavior of the Fe present in the form of atomically dispersed Fe-N_x moieties, which are believed to be the active sites for ORR in acidic medium.[52–54]

Thus, the capacitive current measured by the CV is a combination of various effects, as catalyst surface area, catalyst electrical conductivity, ionomer distribution, catalyst-ionomer interactions, pore geometry and size distribution, and presence of electrochemically active functional groups on the catalyst surface. Since the same catalyst and loading, along with the same fabrication method, were used to prepare the different MEAs, we can reasonably assume that the catalyst surface chemistry is similar and differences in capacitance can be attributed to variations in the electrode microstructure.

The capacitance values for the different electrodes, as reported on Fig. 2c, were calculated starting from the CV data, as the sum of the current density measured at 0.4 V in the positive ($i^{0.4V}_{CV,+}$) and negative ($i^{0.4V}_{CV,-}$) scan directions, divided by two times the scan rate (ν),

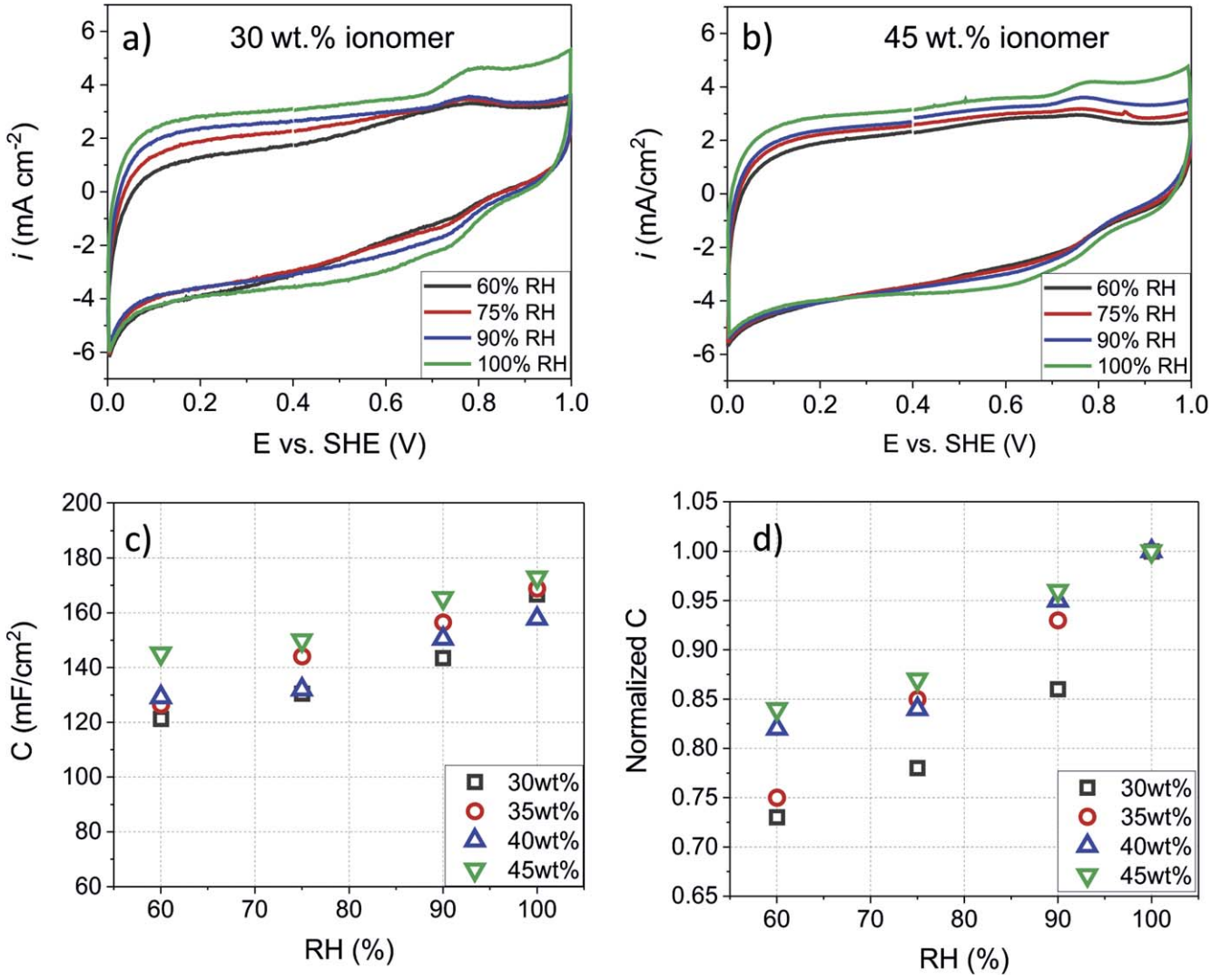

Figure 2. Effect of ionomer loading and RH on the electrode capacitance. (a) CV of the electrode with 30 wt% ionomer loading at different RH; (b) CV of electrode with 45 wt% ionomer loading at different RH; (c) Capacitance in function of RH for the electrodes with different ionomer loadings; (d) Normalized capacitance in function of RH for the electrodes with different ionomer loadings.

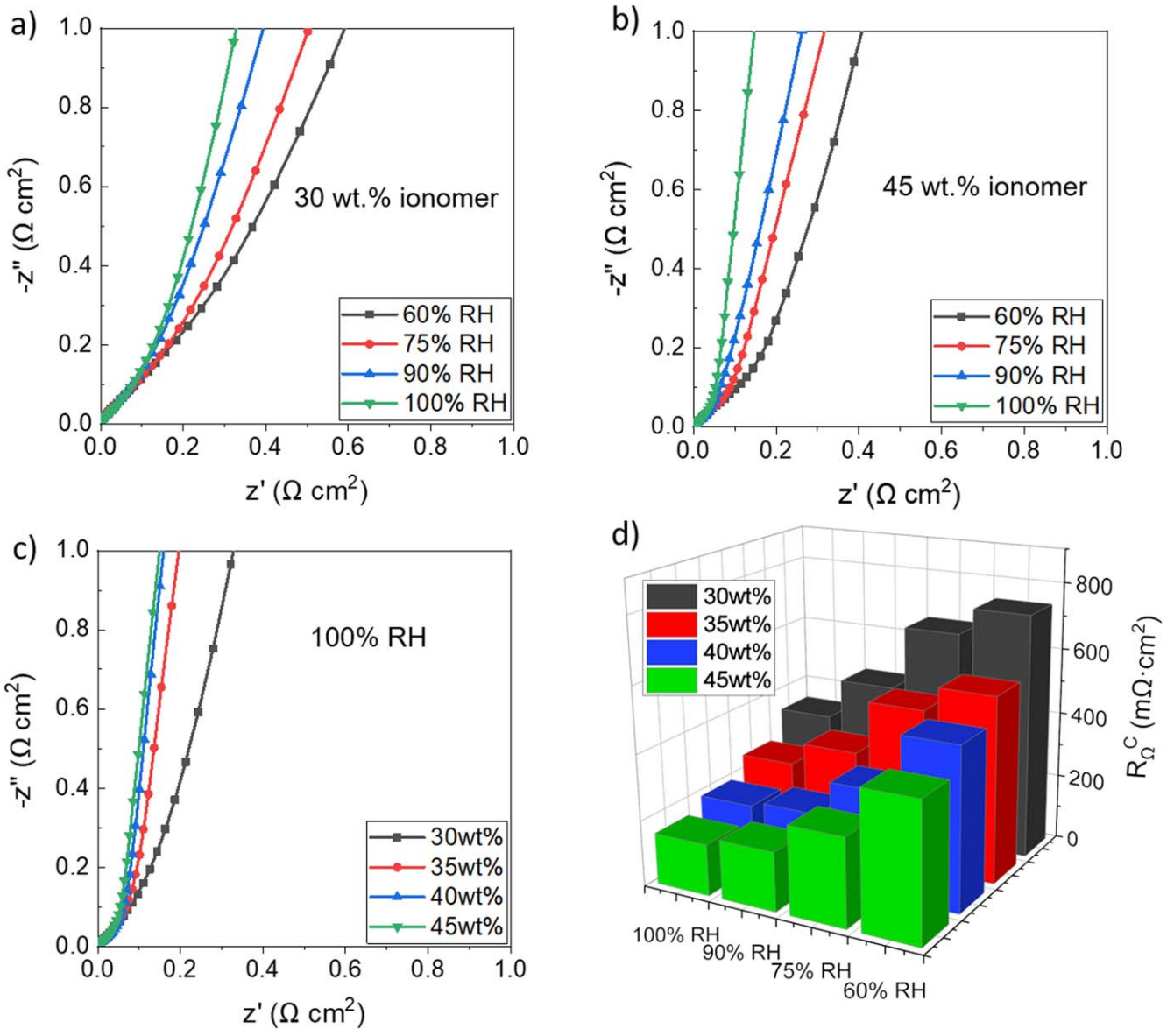

Figure 3. Nyquist plots of the EIS measured under H_2/N_2 at different RH for electrodes with (a) 30 wt% ionomer, and (b) 45 wt% ionomer. (c) Nyquist plots of the EIS measured at 100% RH for the electrodes with different ionomer contents. In all the Nyquist plots the HFR has been subtracted from the real component to better evidence the differences in the ~45° slope region of the different plots. (d) Bar plot representing the $R_\Omega{}^C$ values in function of ionomer content and RH.

according to Eq. 1:

$$C = \frac{i_{CV,+}^{0.4V} + |i_{CV,-}^{0.4V}|}{2\nu} \quad [1]$$

For all the electrodes used in this study, regardless of the ionomer content, the capacitance decreases with the decrease of the RH (Fig. 2c). This can be explained by increased wetting of electrocatalyst surface and pores as RH increases.[42,55] In addition, increasing RH results in ionomer swelling,[41,56] potentially enhancing the interaction between ionomer and catalyst via increased catalyst surface coverage thereby increasing the capacitive response.

As evident from Figs. 2 and S2, the electrodes with different ionomer loadings show very similar capacitance at the high RH values of 90 and 100%, with only the 30% ionomer electrode having a slightly lower capacitance at 90% RH. The situation changes at lower RH values, where larger decreases in capacitance are observed at lower ionomer contents (Fig. 2c). In fact, at lower RH, the 45 wt% ionomer electrode has the highest capacitance, correlating with the increased performance in Fig. 2b.

While the use of absolute capacitance alone would make it difficult to discern the relative interactions of ionomer and water with the electrocatalyst, normalized capacitance can be utilized to glean information about the electrode microstructure and qualitatively demonstrate the level of interaction between the electrolyte (ionomer) and the electrode surface (catalyst).

Figure 2d plots normalized capacitance vs RH for the four electrodes. The normalized capacitance is defined as the capacitance at a certain RH, divided by the capacitance at 100% RH (where the maximum capacitance is observed). Generally speaking, the larger the decrease in normalized capacitance (C at a given RH vs 100% RH), the greater the dependence on liquid water and the relatively lower the interaction between ionomer and electrocatalyst. In the RH range from 60% to 100%, the steeper capacitance decrease with RH is observed for the electrodes with lower ionomer content. In fact, the higher capacitance decrease is observed for the electrode with 30 wt% ionomer, where the normalized capacitance at 60% RH decreases to 73% of the value measured at 100% RH. On the other hand, smaller capacitance decreases are observed for electrodes prepared with 40 and 45 wt% ionomer. This behavior is reasonable,

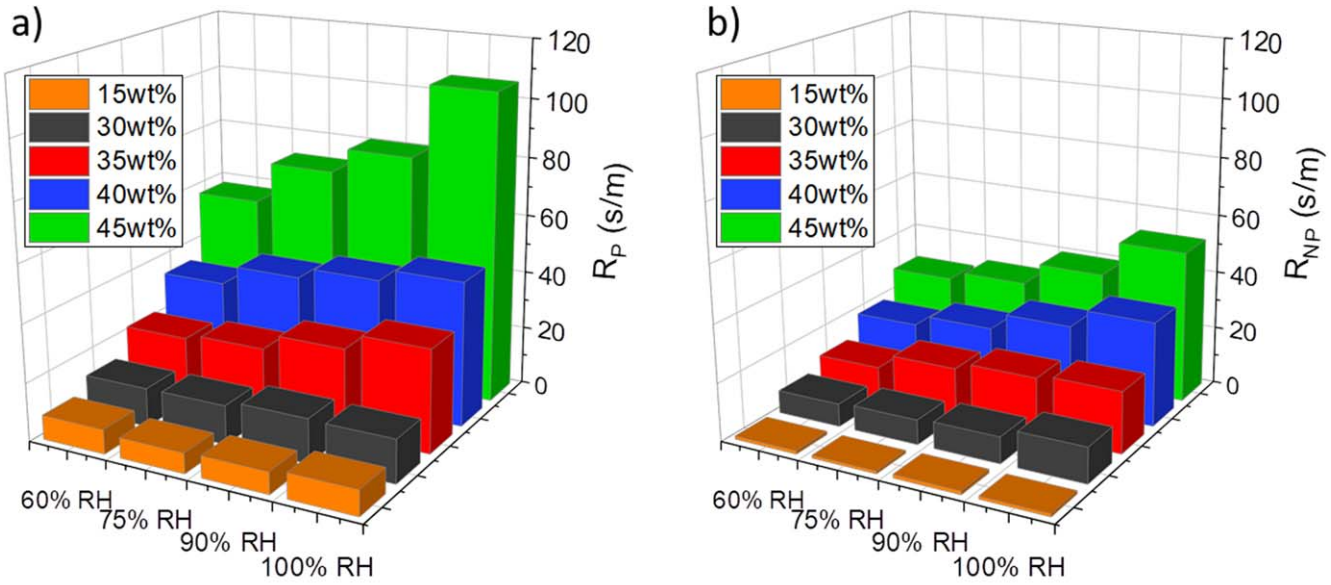

Figure 4. Mass transport properties for PGM-free catalyst layers with different ionomer contents at different RH. (a) Pressure dependent component due to molecular diffusion (R_P) measured at 150 kPa; (b) pressure independent component due to Knudsen diffusion (R_{NP}).

considering that an electrode with a lower ionomer content would provide a lower ionomer surface coverage of the electrocatalyst, becoming more sensitive to capillary condensation and the presence of liquid water. To the contrary, having more ionomer facilitates more coverage of the electrocatalyst, reducing the dependence on RH.

Electrochemical impedance spectroscopy.—Figure 3 shows the EIS Nyquist plots of the CCLs measured at different RH. According to the transmission line model described in several publications[44,45] (equivalent circuit shown in Fig. S1) the ca. 45° slope from the H_2/N_2 EIS Nyquist plot relates to the electrode proton resistance. The transmission line model was used to fit the experimental EIS data measured for the four electrodes with the different ionomer contents across a range of RHs and extract their respective cathode proton resistance ($R_\Omega{}^C$, defined in Eq. 2, where δ_{cl} is cathode catalyst layer thickness, σ_i is ionomer conductivity, and ε_i is the ionomer volume fraction). The resulting $R_\Omega{}^C$ values are shown in Table I, with the trend as a function of RH and ionomer content in the electrode is more clearly depicted in Fig. 3d.

$$R_\Omega^C = \frac{\delta_{cl}}{\sigma_i \varepsilon_i} \quad [2]$$

As evident from the values in Table I and from the shape of the Nyquist plots in Figs. 3 and S3, the proton resistance in the CCL increases with the decrease of the RH. At higher RH, both the increased water uptake of the ionomer as well as the increased condensation of liquid water in the small pores of the electrode and electrocatalyst increase the network of proton conduction through the CCL. For all the MEAs, the $R_\Omega{}^C$ values measured at 60% RH are between 2.2 to 2.7 times higher than the values measured at 100% RH. At 75% RH the $R_\Omega{}^C$ values are only 1.4 to 2 times higher, while at 90% RH only 1.1 to 1.4 times.

If we observe the plot in Fig. 3c and the values in Table I, we notice that at the same RH value, the MEAs with the higher ionomer content have the lower CCL proton resistance. This trend is explicable by having a larger and less tortuous ionomer path, less dependent on hydration, ionomer swelling and the presence of liquid water to enable protons conduction throughout the CCL.

Mass transport resistance.—The HOR limiting current densities were obtained from CVs for the electrodes with different ionomer contents, deposited on the PtB sensor layer. A schematic of the cell assembly used in this work along with the relevant derivations are shown in Ref. 40 (see Fig. 1 in Ref. 40 for cell assembly). The limiting current densities and values for the total transport resistance through the bulk electrode, i.e. from the DM side to the membrane side, represented by R_{total}, are shown in Fig. S4 and calculated by Eq. 3.

$$R_{measured} = R_b + R_{total} = \frac{nFC_{H_2,channel}}{i_{lim,ob} - i_x - i_{CV}} \quad [3]$$

Here, $R_{measured}$ is the measured transport resistance through the entire cell, R_b is the background resistance in the absence of a PGM-free catalyst layer, n is the number of electrons transferred by reaction, F is Faraday's constant, $C_{H_2,channel}$ is the H_2 concentration in the flow field channel, $i_{lim,ob}$ is the measured limiting current, i_x is the crossover current, and i_{CV} is the background current of the H_2 limiting current set up from cyclic voltammetry in N_2.

Table I. Proton resistance ($R_\Omega{}^C$) in the CCL of the MEAs with different ionomer contents obtained from the EIS data measured at different RH fitted with the transmission line circuit model.

	$R_\Omega{}^C$ (mΩ·cm^2)			
Ionomer in the CCL (wt%)	60% RH	75% RH	90% RH	100% RH
30	740	659	464	339
35	560	487	323	253
40	488	314	208	193
45	413	267	178	155

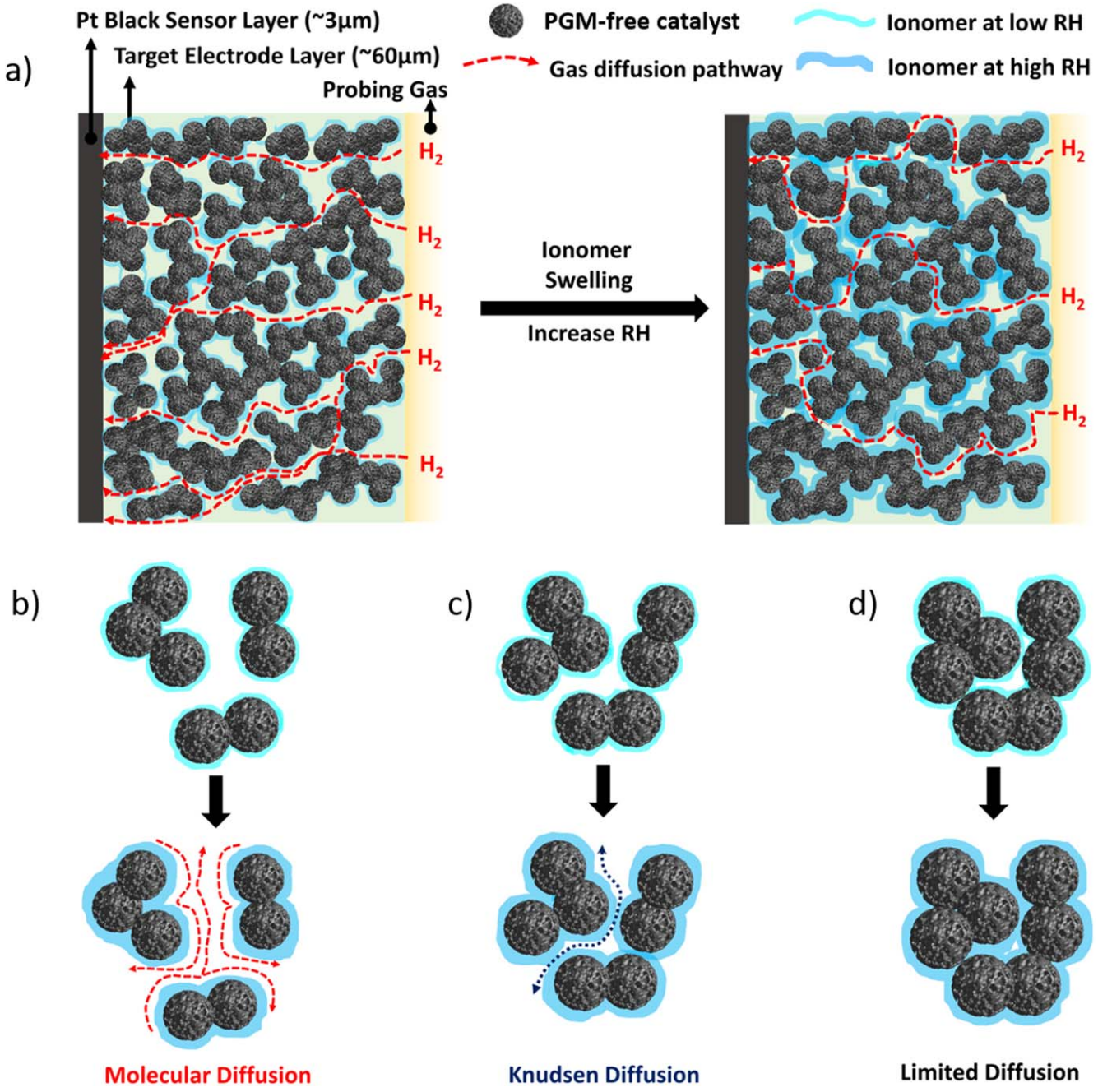

Figure 5. Scheme representing the impact of increasing RH and ionomer content on gas transport properties of a PGM-free electrode. (a) Ionomer swelling and increase of tortuosity; (b) molecular diffusion; (c) Knudsen diffusion; (d) limited diffusion.

R_{total} can be broken down into two separate components; a pressure-dependent resistance (R_P), stemming from molecular diffusion, and a pressure-independent resistance (R_{NP}), resulting from Knudsen diffusion through smaller pores and solid-state diffusion through ionomer films. R_P can be obtained from values derived from the linear trend of R_{total} as a function of pressure, while the ordinate intercept represents R_{NP}. Since the GDL resistance is measured in R_b, it does not contribute to either R_P or R_{NP}.

Figures S4a and S4b show HOR limiting current and R_{total} as a function of both pressure and RH. R_{total} is subsequently broken down into R_P and R_{NP} in Fig. 4. The first clear trend in Fig. 4 is the rapidly increasing values of R_P with ionomer content (Fig. 4a) and to a lesser extent the increase in R_{NP} (Fig. 4b). The thicknesses were the same for the catalyst layers with different ionomer loadings, i.e. 48 ± 2 μm. When the ionomer loading in the catalyst layer increases, the total electrode thickness does not increase but instead more pore volume is occupied, resulting in a more tortuous pathway for molecular diffusion. In addition, because the pressure dependent and independent pathways for diffusion through the thickness of the catalyst later occur both in parallel and series, the increased narrowing of pores due to ionomer aggregation results in a simultaneous increase in both R_P and R_{NP}.

At the lowest ionomer content (15 wt%) both R_P and R_{NP} do not change as a function of RH, since the ionomer volume fraction is just over ~5% in this case (based on a carbon density of 2 g cm^{-3} and an ionomer density of 1.6 g cm^{-3}). As ionomer content and volume fraction are increased, however, R_{NP} first increases moderately with RH, for 30 and 35 wt% ionomer, and then drastically for 40 and 45 wt%. The increase in R_{NP} values with increasing RH for the bulk electrode is notably different than what was previously observed for

aggregate level transport resistance through ionomer films in PGM-free electrodes.[21] In their study, Ahluwalia and co-workers showed decreasing transport resistance through ionomer films surrounding the PGM-free electrocatalyst as RH increased. Since the study presented here probes transport resistance through only the thickness of the electrode layer, it does not consider any resistances accessing the electrocatalyst active site.

As mentioned before, R_{NP} includes contributions from Knudsen diffusion, which is mainly related to the transport resistance inside micropores, and solid-state diffusion, through ionomer films. As ionomer loading increases it occupies more macropore volume, altering the balance of macro and microporosity in the electrode, increasing R_{NP} as well as RH sensitivity due to enhanced water uptake and swelling on a volumetric basis. The swelled ionomer occupies more space and closes off, or greatly reduces macro and micropore accessibility, subsequently increasing the tortuosity of the molecular pathway, depicted in Fig. 5a. Other reasons for the observed mass transport resistance increase with RH can be the presence of some liquid water on hydrophilic nucleation sites even at RH $<$ 100%, and the decrease in the diffusivity coefficient of H_2 in the gas as the H_2O molar fraction increases. Nevertheless, at high ionomer loading (e.g. 45 wt%), the fuel cell operation at 100% RH may have considerable mass transport limitations, as confirmed by the polarization curves results in Fig. 1c.

In addition to the case of high vs low RH, Fig. 5 could also represent the case of lower ionomer content vs higher ionomer content (at the same RH). In Fig. 5a, the left side could represent the electrode with low ionomer content (e.g. 30 wt%), and the right side could represent the high ionomer content one (e.g. 45 wt%). In Figs. 5b–5d, the upper and lower portions represent low and high ionomer content electrodes, respectively. It is obvious that when the ionomer loading increases, the total pore size and void volume of the electrode decreases, and the pathway for the gases to reach the active sites becomes more tortuous. As a result, the transport resistance of the electrode increases. In addition, when the ionomer loading increases, the connectivity of the ionomer network increases, favoring the proton conduction through the CL.

Interpretation of fuel cell performances using MEA diagnostics results.—Analyzing the results obtained in this work, one should consider that the ORR in the cathode of a PEFC takes place on a triple-phase boundary region at the conjunction of active sites, proton accessibility (being it through liquid water or ionomer), and reactant (O_2 gas diffusing from the cathode flow field to the electrode bulk).[57] To better understand the relationship between cell performance in Fig. 1 and the CCL properties, Fig. 6 shows R_{total} vs $R_\Omega{}^C$ for the four CCLs with different ionomer contents at various RHs.

While the performance in the kinetic region (low current density) is very similar for all the MEAs at both RHs, for H_2/air polarization curves at 100% RH (Fig. 1c), the best performance at high current density was measured for the MEAs with lower ionomer content (30 and 35 wt%). These two MEAs outperform the one with 40 wt% ionomer and to a greater extent the one with 45 wt% ionomer. The same trend is observed for the polarization curves in H_2/air at 75% RH, but with a smaller performance difference at high current density compared to the 100% RH case. This behavior is well explained by Fig. 6. In H_2/air, at high current density, the main limitation for the cathode performance is the O_2 gas mass transport. Thus, the MEAs showing low bulk-electrode mass transport resistance, 30 and 35 wt%, have a better performance. The performance at 100% RH is even more affected by mass transport limitations, due to the presence of liquid water and enhanced ionomer swelling, as shown by the plots in Fig. 4, and represented schematically in Fig. 5. Naturally, depending on the micro and mesoporosity as well as the electrocatalyst and ionomer aggregation in the resulting electrode, there may be additional transport losses up to the active-site, e.g. through the ionomer film and carbon

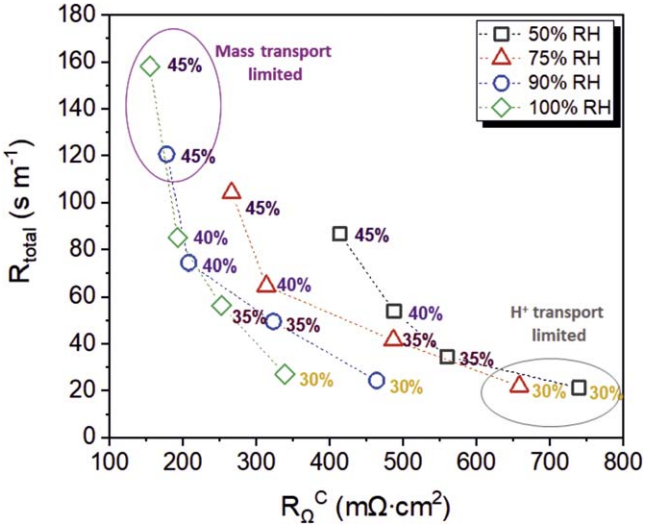

Figure 6. Mass transport resistance (R_{total}) in function of proton resistance in the CL ($R_\Omega{}^C$) for the electrodes with different ionomer contents at the different RH values examined in this work. The values close to each symbol in the plot indicate the ionomer wt% content.

micropores, analogous to those in low-PGM electrodes, which may impact PGM-free electrode performance.

For the H_2/O_2 polarization curves, at 100% RH only the MEA with 35 wt% ionomer slightly outperforms the other MEAs, which are almost all superimposed. Alternatively, at 75% RH the MEA with 45 wt% ionomer shows the slightly higher performance. This is because when pure O_2 is used at the cathode the pressure dependent component of the mass transport resistance is much lower than in air, making performance less sensitive to electrode mass transport. This explains the better performance of the 45 wt% ionomer MEA at low RH, where the performance is therefore more dependent on electrode proton resistance.

Conclusions

A clear correlation was found between the performance of PGM-free based PEFCs as a function of ionomer content ranging from 30% to 45%. The utilization of both novel (H_2 limiting current) and more ubiquitous (CV and EIS) electrochemical diagnostics, revealed a trade-off between proton and bulk electrode gas mass transport resistance (Fig. 6). It was demonstrated that the MEAs performing better at a certain RH values, are the ones showing the best compromise between lower proton and bulk electrode gas mass transport resistance.

While performance improvements greater than 50% were demonstrated for H_2/air operation by tuning ionomer content, advancements beyond those depicted in the "master curve" (Fig. 6) will need to come from improved catalyst accessibility, novel electrode fabrication techniques in terms of catalyst ink formulations and deposition methods,[27,58] and/or improved electrode architectures that decouple proton and gas transport properties.

Acknowledgments

This work was authored by Alliance for Sustainable Energy, LLC, the manager and operator of the National Renewable Energy Laboratory for the U.S. Department of Energy (DOE) under Contract No. DE-AC36-08GO28308. Research performed as part of the Electrocatalysis Consortium (ElectroCat), established as part of the Energy Materials Network, which is supported by the U.S. Department of Energy, Office of Energy Efficiency and Renewable Energy, Fuel Cell Technologies Office (FCTO). The authors wish to thank Dimitrios Papageorgopoulos and Simon Thompson in FCTO at DOE for supporting this work and Min Wang for her assistance providing graphics. While we do not endorse any materials

presented in this study, we wish to thank Alexey Serov and Bar Zulevi of Pajarito Powders LLC for the use of their electrocatalysts. The views expressed in the article do not necessarily represent the views of the DOE or the U.S. Government.

ORCID

Luigi Osmieri https://orcid.org/0000-0002-3111-2270
K. C. Neyerlin https://orcid.org/0000-0002-6753-9698

References

1. R. Baker and J. Zhang, *Electrochemistry Encyclopedia* (2011), http://knowledge.electrochem.org/encycl/art-f04-fuel-cells-pem.htm.
2. K. Vignarooban, J. Lin, A. Arvay, S. Kolli, I. Kruusenberg, K. Tammeveski, L. Munukutla, and A. M. Kannan, *Chinese J. Catal.*, **36**, 458 (2015).
3. D. Banham and S. Ye, *ACS Energy Lett.*, **2**, 629 (2017).
4. S. Thompson and D. Papageorgopoulos, *Nature Catalysis*, **7**, 558 (2019).
5. California Air Resources Board, *Annual Evaluation of Fuel Cell Electric Vehicle Deployment & Hydrogen Fuel Station Network Development* (2018), https://ww2.arb.ca.gov/sites/default/files/2018-12/ab8_report_2018_print.pdf.
6. T. Nguyen, Z. Abdin, T. Holm, and W. Merida, *Energy Conversation and Management*, **200**, 112108 (2019).
7. C. Thiel, J. Schmidt, A. Van Zyl, and E. Schmid, *Transportation Research Part (Part A)*, **63**, 25 (2014).
8. F. Jaouen, E. Proietti, M. Lefèvre, R. Chenitz, J.-P. Dodelet, G. Wu, H. T. Chung, C. M. Johnston, and P. Zelenay, *Energy Environ. Sci.*, **4**, 114 (2011).
9. Z. Chen, D. Higgins, A. Yu, L. Zhang, and J. Zhang, *Energy Environ. Sci.*, **4**, 3167 (2011).
10. U. Martinez, S. Komini Babu, E. F. Holby, H. T. Chung, X. Yin, and P. Zelenay, *Adv. Mater.*, 1806545 (2019).
11. J. Li and F. Jaouen, *Curr. Opin. Electrochem.*, **9**, 198 (2018).
12. G. Wu and P. Zelenay, *Acc. Chem. Res.*, **46**, 1878 (2013).
13. A. A. Gewirth, J. A. Varnell, and A. M. Diascro, *Chem. Rev.*, **118**, 2313 (2018).
14. L. Osmieri, *ChemEngineering*, **3**, 16 (2019).
15. M. Shao, Q. Chang, J.-P. Dodelet, and R. Chenitz, *Chem. Rev.*, **116**, 3594 (2016).
16. X. Yin, L. Lin, H. T. Chung, S. Komini Babu, U. Martinez, G. M. Purdy, and P. Zelenay, *ECS Trans.*, **77**, 1273 (2017).
17. L. Osmieri, R. Escudero-Cid, A. H. A. Monteverde Videla, P. Ocón, and S. Specchia, *Appl. Catal. B Environ.*, **201**, 253 (2017).
18. S. Komini Babu, H. T. Chung, P. Zelenay, and S. Litster, *ACS Appl. Mater. Interfaces*, **8**, 32764 (2016).
19. A. Kongkanand and M. F. Mathias, *J. Phys. Chem. Lett.*, **7**, 1127 (2016).
20. H. M. Barkholtz, L. Chong, Z. B. Kaiser, T. Xu, and D.-J. Liu, *Catalysts*, **5**, 955 (2015).
21. R. K. Ahluwalia, X. Wang, L. Osmieri, J.-K. Peng, H. T. Chung, and K. C. Neyerlin, *J. Electrochem. Soc.*, **166**, F1096 (2019).
22. A. Kriston, T. Xie, and B. N. Popov, *Electrochim. Acta*, **121**, 116 (2014).
23. K. B. Hatzell, M. B. Dixit, S. A. Berlinger, and A. Z. Weber, *J. Mater. Chem. A*, **5**, 20527 (2017).
24. S. A. Mauger, K. C. Neyerlin, A. C. Yang-Neyerlin, K. L. More, and M. Ulsh, *J. Electrochem. Soc.*, **165**, F1012 (2018).
25. F. C. Cetinbas, S. G. Advani, and A. K. Prasad, *J. Power Sources*, **270**, 594 (2014).
26. S. Khandavalli, J. H. Park, N. N. Kariuki, D. J. Myers, J. J. Stickel, K. Hurst, K. C. Neyerlin, M. Ulsh, and S. Mauger, *ACS Appl. Mater. Interfaces*, **10**, 43610 (2018).
27. L. Osmieri, S. A. Mauger, M. Ulsh, K. C. Neyerlin, and G. Bender, *J. Power Sources*, **452**, 227829 (2020).
28. T. T. Ngo, T. L. Yu, and H. L. Lin, *J. Power Sources*, **238**, 1 (2013).
29. F. C. Cetinbas and R. K. Ahluwalia, *J. Electrochem. Soc.*, **165**, F1059 (2018).
30. K. C. Neyerlin, W. Gu, J. Jorne, A. Clark, and H. A. Gasteiger, *J. Electrochem. Soc.*, **154**, B279 (2007).
31. H. K. Lee, J. H. Park, D. Y. Kim, and T. H. Lee, *J. Power Sources*, **131**, 200 (2004).
32. H. A. Gasteiger, S. S. Kocha, B. Sompalli, and F. T. Wagner, *Appl. Catal. B Environ.*, **56**, 9 (2005).
33. M. Lefèvre, E. Proietti, F. Jaouen, and J.-P. Dodelet, *Science*, **324**, 71 (2009).
34. K. Karan, *Curr. Opin. Electrochem.*, **5**, 27 (2017).
35. D. R. Baker, D. A. Caulk, K. C. Neyerlin, and M. W. Murphy, *J. Electrochem. Soc.*, **156**, B991 (2009).
36. F. B. Spingler, A. Phillips, T. Schuler, M. C. Tucker, and A. Z. Weber, *Int. J. Hydrogen Energy*, **42**, 13960 (2017).
37. T. Schuler, A. Chowdhury, A. T. Freiberg, B. Sneed, F. B. Spingler, M. C. Tucker, K. L. More, C. J. Radke, and A. Z. Weber, *J. Electrochem. Soc.*, **166**, F3020 (2019).
38. T. A. Greszler, D. Caulk, and P. Sinha, *J. Electrochem. Soc.*, **159**, F831 (2012).
39. N. Nonoyama, S. Okazaki, A. Z. Weber, Y. Ikogi, and T. Yoshida, *J. Electrochem. Soc.*, **158**, B416 (2011).
40. Y. Ono, A. Ohma, K. Shinohara, and K. Fushinobu, *J. Electrochem. Soc.*, **160**, F779 (2013).
41. A. Z. Weber et al., *J. Electrochem. Soc.*, **161**, 1254 (2014).
42. E. Frackowiak and F. Béguin, *Carbon*, **39**, 937 (2001).
43. L. Osmieri, A. H. A. Monteverde Videla, and S. Specchia, *J. Solid State Electrochem.*, **20**, 3507 (2016).
44. G. Li and P. G. Pickup, *J. Electrochem. Soc.*, **150**, C745 (2003).
45. R. Makharia, M. F. Mathias, and D. R. Baker, *J. Electrochem. Soc.*, **152**, A970 (2005).
46. A. G. Star, G. Wang, S. Medina, S. Pylypenko, and K. C. Neyerlin, *J. Power Sources*, **450**, 227655 (2020).
47. S. Kabir, D. J. Myers, N. N. Kariuki, J. Park, G. Wang, N. Macauley, R. Mukundan, K. L. More, and K. C. Neyerlin, *ACS Appl. Mater. Interfaces*, **11**, 45016 (2019).
48. A. Orfanidi, P. J. Rheinländer, N. Schulte, and H. A. Gasteiger, *J. Electrochem. Soc.*, **165**, F1254 (2018).
49. T. Kim, S. Lim, K. Kwon, S. H. Hong, W. Qiao, C. K. Rhee, S. H. Yoon, and I. Mochida, *Langmuir*, **22**, 9086 (2006).
50. J. Wang, G. Yin, Y. Shao, S. Zhang, Z. Wang, and Y. Gao, *J. Power Sources*, **171**, 331 (2007).
51. J. S. M. Lee, M. E. Briggs, C. C. Hu, and A. I. Cooper, *Nano Energy*, **46**, 277 (2018).
52. L. Birry, J. H. Zagal, and J. P. Dodelet, *Electrochem. Commun.*, **12**, 628 (2010).
53. L. Osmieri et al., *Appl. Catal. B Environ.*, **257**, 117929 (2019).
54. Q. Jia et al., *ACS Nano*, **9**, 12496 (2015).
55. J. Y. Choi, L. Yang, T. Kishimoto, X. Fu, S. Ye, Z. Chen, and D. Banham, *Energy Environ. Sci.*, **10**, 296 (2017).
56. L. Xing, P. K. Das, X. Song, M. Mamlouk, and K. Scott, *Appl. Energy*, **138**, 242 (2015).
57. H. M. Barkholtz and D.-J. Liu, *Mater. Horizons*, **4**, 20 (2017).
58. T. Van Cleve et al., *ACS Appl. Mater. Interfaces*, **11**, 46953 (2019).